Invariant Crease Lines for Topological and Structural Analysis of Tensor Fields

Xavier Tricoche, *Member, IEEE*, Gordon Kindlmann, and Carl-Fredrik Westin

Abstract—We introduce a versatile framework for characterizing and extracting salient structures in three-dimensional symmetric second-order tensor fields. The key insight is that degenerate lines in tensor fields, as defined by the standard topological approach, are exactly crease (ridge and valley) lines of a particular tensor invariant called mode. This reformulation allows us to apply well-studied approaches from scientific visualization or computer vision to the extraction of topological lines in tensor fields. More generally, this main result suggests that other tensor invariants, such as anisotropy measures like fractional anisotropy (FA), can be used in the same framework in lieu of mode to identify important structural properties in tensor fields. Our implementation addresses the specific challenge posed by the non-linearity of the considered scalar measures and by the smoothness requirement of the crease manifold computation. We use a combination of smooth reconstruction kernels and adaptive refinement strategy that automatically adjust the resolution of the analysis to the spatial variation of the considered quantities. Together, these improvements allow for the robust application of existing ridge line extraction algorithms in the tensor context of our problem. Results are proposed for a diffusion tensor MRI dataset, and for a benchmark stress tensor field used in engineering research.

Index Terms—Tensor fields, tensor invariants, ridge lines, crease extraction, structural analysis, topology.

---

1 INTRODUCTION

Despite the fundamental importance of tensor fields in the description of a variety of phenomena in science, engineering, and medicine, the analysis of the corresponding data remains a challenging problem. In particular, the ability to effectively represent the information encoded in tensor datasets remains the elusive goal of a significant body of research in the scientific visualization community.

In the variety of tensor visualization techniques proposed in the literature, those that allow for an automatic characterization of important structural properties are especially useful because they lend themselves to an offline post-processing of the datasets routinely acquired through measurements or numerical simulations. In applications ranging from solid mechanics and fluid dynamics to medical imaging, the ability to convey the salient contents of tensor fields to the user without a time-consuming search is crucial to the task of domain experts.

In recent years, several publications by Zheng and Pang have contributed a theoretical and algorithmic topological framework to the analysis and visual representation of tensor fields [42, 43]. Specifically, their work has clarified the dimensionality of so-called degenerate tensors, showing that the singularities of the topology typically constitute lines in the tensor setting. Additionally, these authors have proposed a method that automatically computes the corresponding skeleton, yielding a synthetic and compact representation of the tensor data. While this approach achieves very compelling results in the case of smooth datasets exhibiting a high degree of symmetry, some authors recently showed that the topology is a fragile structure and as such not directly relevant to the structural analysis of noisy measurement data like Diffusion Tensor MRI (DTI) [38].

These observations provide the general context and the motivation of the work presented in this paper. We describe a methodology grounded on objective principles that inherits the virtue of automatic structural extraction and abstract representation of the topological approach while addressing its practical shortcomings in applications confronted to noisy data. In particular, we show that the singularities of tensor topology constitute a special case of a general formalism based on the notion of crease lines of tensor invariants. An important benefit of this reformulation is that previous work on the extraction of crease manifolds in image processing and computer vision can be leveraged to facilitate the computation of the corresponding features.

More precisely, we explain in the following how a quantity present in the continuum mechanics literature called *mode* exactly characterizes the singular behavior of tensor fields. Hence, if topology is the focus of the data analysis problem, the ridge and valley lines of mode can be extracted from tensor fields using crease line extraction schemes to yield the desired degenerate lines. More importantly, considering tensor topology from this perspective suggests that the crease lines of other tensor invariants can be substituted to mode in the same versatile framework to yield an insightful picture of the important structural properties present in the data. One significant example that we consider in the following concerns the fractional anisotropy (FA) commonly used in the analysis of DTI data. Our results show that the ridge lines of FA capture certain important white matter tracts. Another important contribution of this paper, which provides the algorithmic foundation of our crease-based approach, is a robust and accurate method for the extraction of these feature lines from nonlinear quantities. Indeed, measures like mode and FA are nonlinear invariants whose computation from the tensor coefficients requires caution. Since the definition of ridge and valley lines involves the first and second-order derivatives of the considered scalar measure, our implementation uses smooth reconstruction kernels in the computation of tensor invariants. Additionally, we combine these kernels with an adaptive scheme that automatically adjusts the resolution of the crease line extraction to the spatial variations of the invariant. As a result our method permits the application of existing crease line extraction schemes to the structural analysis of tensor fields. Our new framework is algorithmically simpler and also theoretically more general, since it allows for the definition of structural saliency in terms of several invariants that can be naturally adapted to the focus of a particular application.

The remainder of this paper is organized as follows. Related work, with emphasis on topological methods for tensor fields and crease manifolds in image data is discussed in Section 2. Our presentation proceeds by reviewing fundamental theoretical notions relevant to this work in Section 3. Implementation considerations, centered around the specific challenges posed by the nonlinearity of tensor invariants and by their smooth reconstruction, are detailed in Section 4. Results

- *Xavier Tricoche is with the Computer Science Department, Purdue University, E-mail: xmt@purdue.edu.*
- *Gordon Kindlmann is with Brigham and Women's Hospital, Harvard Medical School, E-mail: gk@bwh.harvard.edu.*
- *Carl-Fredrik Westin is with Brigham and Women's Hospital, Harvard Medical School, E-mail: westin@bwh.harvard.edu.*

are proposed in Section 5 for a synthetic dataset of a stress tensor field on one hand and for a DTI dataset of the brain white matter on the other hand. We conclude by discussing our findings and mentioning interesting avenues to extend this work in Section 6.

2 RELATED WORK

The research presented in this paper is closely related to previous work on tensor field topology visualization and crease detection in image data.

2.1 Topological Methods

The topological framework was first applied to the visualization of second-order tensor field by Delmarcelle and Hesselink [6]. Leveraging ideas introduced previously for the topology-based visualization of vector fields [16, 13], these authors proposed to display a planar tensor field through the topological structure of its two orthogonal eigenvector fields. As discussed in their work, the lack of orientation of eigenvector fields leads to singularities that are not seen in regular vector fields. Those *degenerate points* correspond namely to locations where the tensor field becomes isotropic, i.e. where both eigenvalues are equal and the eigenvectors are undefined. Yet, this seminal work shows that a similar synthetic representation is obtained in the tensor setting through topological analysis: degenerate points are connected in graph structure through curves called *separatrices* that are everywhere tangent to an eigenvector field.

The three-dimensional case was first considered in a subsequent paper by Hesselink *et al.* [17]. Interestingly, their discussion was primarily focused on the types of degenerate *points* that can occur in this setting. As such it did not explicitly mention that the most typical singularities in 3D are lines and not isolated points. In fact, this basic property was first pointed out in the work of Zheng and Pang [42] who also proposed the first algorithm for the extraction of these line features. In a nutshell, their method consists in computing the intersection of these lines with the faces of a voxel grid, by solving a set of 7 cubic equations. This method was later improved by allowing for the continuous tracking of intersection points across the voxel interior [43]. Additionally, a geometric formulation was proposed as an alternative to the system of equations [43]. Most recently, Schultz *et al.* discussed three-dimensional tensor field topology in the context of DT-MRI data [38]. Following a systematic approach, their work demonstrates the shortcomings of this mathematical framework in the structural analysis of the typically noisy images acquired in practice. As an alternative, they proposed an approach where structure is defined with respect to a stochastic assessment of the connectivity along integral curves.

2.2 Crease Features in Image Data

The detection of creases, in other words ridges and valleys, in scalar images is a topic of traditional interest in a variety of disciplines, most prominently in image processing and computer vision [22]. Among the multiple definitions proposed in the literature over the last century [5, 15, 25], the one introduced by Eberly *et al.* is widely used in practice [7]. In essence, this definition generalizes the intuitive height-based definition of ridges and valleys [5] to d-dimensional manifolds embedded in n-dimensional image space [9].

From an algorithmic standpoint, several methods have been proposed that permit the extraction of these manifolds from numerical data. Many of them apply a principle similar to Marching Cubes [23], effectively interpreting creases as 0-level sets of the dot product between the gradient of the considered scalar image and one or several eigenvectors of its hessian matrix. The lack of intrinsic orientation of those eigenvectors requires the use of heuristics to provide them with an arbitrary but locally consistent orientation. Some authors match sets of eigenvectors across the faces of a voxel [28, 12] while others determine a local reference by computing the average orientation of the eigenvector field over a face [39, 11]. A scale-space approach is discussed in [12]. Peikert and Roth introduced the notion of *Parallel Vector Operator* [32] as a computation primitive in flow visualization and they showed that it could be used to find the intersection of ridge

and valley lines with the faces of a computational mesh [34]. Computationally, the method can be implemented in a variety of ways, including isocontour intersection, iterative numerical search, and through the solution of an eigensystem.

It is interesting to observe that several applications of this general methodology to Scientific Visualization problems have been presented in recent years. Sahner *et al.* extract a skeleton of vortices in three-dimensional flows as valley lines of a galilean invariant called λ_2 [36]. Their algorithm combines ideas developed by Eberly with a *Feature Flow Field* approach [40]. In a work most closely related to ours, Kindlmann *et al.* extract ridge and valley surfaces of the *Fractional Anisotropy* (FA) in DTI volumes using a modified version of *Marching Cubes*. In particular, their scheme uses smooth reconstruction kernels and an orientation tracking scheme along edges to assign a coherent orientation to an eigenvector field on a voxel face. Most recently, Sadlo and Peikert applied the scheme proposed by Furst and Pizer [11] to extract *Lagrangian Coherent Structures* from transient flows as ridge and valley surfaces of a scalar measure of particle coherence [35].

3 THEORETICAL BACKGROUND

We start our presentation of the theory by summarizing basic definitions of tensor topology, which we use to put our work in the perspective of existing techniques. We proceed by discussing the notion of tensor invariants and finally describe how a geometric structure can be derived from those invariants in a practical setting.

3.1 Tensor Field Topology

It is well known that any three-dimensional second-order symmetric tensor (simply called *tensor* in the following) is equivalently represented by three real eigenvalues and an associated set of three mutually orthogonal eigenvectors. For a tensor field, the ordering of the three eigenvalues $\lambda_1 \geq \lambda_2 \geq \lambda_3$ therefore defines three (so-called *major*, *medium*, and *minor*) eigenvector fields. In each eigenvector field, curves can be constructed that are everywhere tangent to the field. These curves are generally referred to as *hyperstreamlines* in the visualization literature [6].

This basic setting allows us to define the topology of a tensor field in terms of the connectivity established along hyperstreamlines. In other words, topology segments the domain into regions where hyperstreamlines share the same end locations. This formalism is directly related to the topological framework used to study vector fields, where it characterizes regions of similar asymptotic behavior of the corresponding flow [37]. In the tensor setting, *singularities* of the topology corresponds to locations where the directional information of an eigenvector field is degenerate, which occurs when two or more eigenvalues are equal. It follows that three degenerate configurations are possible in the three-dimensional case, namely $\lambda_1 = \lambda_2 > \lambda_3$ (sometimes called *planar anisotropy*), $\lambda_1 > \lambda_2 = \lambda_3$ (referred to as *cylindrical anisotropy*), and $\lambda_1 = \lambda_2 = \lambda_3$ (*spherical isotropy*). While the latter case is in fact numerically unstable and typically absent from practical datasets, the first two degeneracies are stable features of the tensor topology. In their recent work Zheng and Pang have shown that these features are in general lines [42, 43], clarifying the picture first offered by Hesselink et al. in their seminal work on 3D tensor topology [17].

From a visualization standpoint, the first algorithm proposed by Zheng and Pang to compute this one-dimensional topological skeleton is quite involved. Specifically, it requires to simultaneously find the roots of 7 constraint functions [42]. These functions correspond to a reformulation of a polynomial minimization problem of degree 6 into a 7D cubic root finding problem that can be solved iteratively on the faces of the 3D grid using a least squares formulation of the Newton-Raphson method [33]. Despite the apparent complexity of this formulation, the authors reported the fast convergence of their method on the voxel faces of synthetic and simulation datasets [42]. In a subsequent paper, Zheng et al. introduced an alternative solution based on the representation of a tensor as the sum of an isotropic (spherical) component and a so-called linear component [43]. In this case, the extraction of degenerate points on voxel faces is based on an iterative

numerical search that requires the inversion of 5x5 matrix at each iteration. Additionally, the efficiency of the initial method was improved by tracking intersections points along a degenerate line, based on the computation of its local tangent [43].

Beside its relative computational complexity, another drawback of the topological approach lies in its lack of robustness. Indeed, the structures identified by a topological analysis were shown to be very sensitive to noise and therefore essentially meaningless in the context of Diffusion Tensor Imaging (DTI), where a low signal-to-noise ratio is typical in clinical practice [38]. This result echoes our observation that alternative structure definitions are needed to address the visual analysis needs of a variety of problems. We illustrate this point with our results on FA in DTI in Section 5.

3.2 Tensor Invariants

Invariants of second-order three-dimensional tensors can be intuitively understood as measurements of tensor *shape*, which is independent of tensor *orientation*. Invariants can be functionally defined in terms of the tensor eigenvalues, or as functions of the coefficients of the matrix representation of a tensor (in, for example, an orthonormal frame). Our implementations use the latter approach to avoid the computational expense of eigenvalue determination, and to facilitate the computation of the spatial derivatives (gradient and Hessian) of invariants, although some observations about the properties of invariants can be made more directly in terms of eigenvalues.

For tensor field topology, the invariant most connected to lines of degeneracy (where two eigenvalues are equal) is *mode*, which was described in continuum mechanics by Criscione et al. [4] and in diffusion tensor imaging by Ennis and Kindlmann [10]. The mode of tensor $\mathbf{D}$ is essentially the skewness of the set of three eigenvalues $\lambda_1 \geq \lambda_2 \geq \lambda_3$ of $\mathbf{D}$

$$\text{mode}(\mathbf{D}) = \sqrt{2}\,\text{skewness}(\lambda_1, \lambda_2, \lambda_3) = \sqrt{2}\frac{\mu_3}{\sqrt{\mu_2}^3} \quad (1)$$

$$\mu_1 = \sum_i \lambda_i/3 \quad (2)$$

$$\mu_2 = \sum_i (\lambda_i - \mu_1)^2/3 \quad (3)$$

$$\mu_3 = \sum_i (\lambda_i - \mu_1)^3/3. \quad (4)$$

As can be easily verified, mode is $+1$ when $\lambda_1 > \lambda_2 = \lambda_3$ and mode is -1 when $\lambda_1 = \lambda_2 > \lambda_3$. Also, the skewness of any three numbers is bounded to $[-1/\sqrt{2}, 1/\sqrt{2}]$. Thus, equality of any two tensor eigenvalues implies that mode is at an extremum ($+1$ or -1). Our implementation uses an equivalent definition of mode [10] in terms of the determinant $\det(\cdot)$, norm $|\cdot|$, and trace $\text{tr}(\cdot)$ of the deviatoric [3] $\widetilde{\mathbf{D}}$ of tensor $\mathbf{D}$

$$\text{mode}(\mathbf{D}) = 3\sqrt{6}\det\left(\frac{\widetilde{\mathbf{D}}}{|\widetilde{\mathbf{D}}|}\right) \quad (5)$$

$$\widetilde{\mathbf{D}} = \mathbf{D} - \text{tr}(\mathbf{D})\mathbf{I}/3 \quad (6)$$

$$|\widetilde{\mathbf{D}}| = \sqrt{\text{tr}(\widetilde{\mathbf{D}}\widetilde{\mathbf{D}}^T)}. \quad (7)$$

where $\mathbf{I}$ is the identity tensor. We find this direct connection between topological degeneracy and a well understood tensor invariant like mode to be intuitive and as such very appealing. In particular, this natural connection contrasts with the rather involved numerical solution proposed previously, where degenerate lines are characterized through expressions derived from the discriminant of the tensor [42] and its Hessian [43].

One way to appreciate the relationship between the extrema of tensor mode, and the equality of two eigenvalues, is to inspect the formulae for the solution of the sorted eigenvalues λ_i in terms of their central moments μ_i:

$$\begin{aligned} \lambda_1 &= \mu_1 + \sqrt{2\mu_2}\cos(\Theta) \\ \lambda_2 &= \mu_1 + \sqrt{2\mu_2}\cos(\Theta - 2\pi/3) \\ \lambda_3 &= \mu_1 + \sqrt{2\mu_2}\cos(\Theta + 2\pi/3) \end{aligned} \quad (8)$$
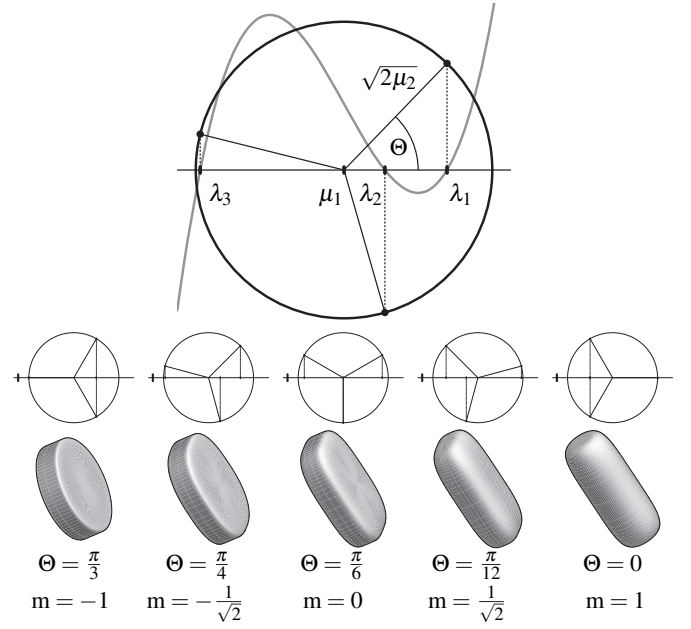

Fig. 1. The eigenvalue wheel provides geometric intuition for why two tensor eigenvalues λ_i are equal when tensor $\text{mode} = m$ is at extremal values ± 1, as governed by $\text{mode} = m = \cos(3\Theta)$. The glyphs illustrate tensors with eigenvalues determined by the wheel.

where $\Theta = \frac{1}{3}\cos^{-1}\left(\frac{\sqrt{2}\mu_3}{\sqrt{\mu_2}^3}\right)$. This can be derived from the solution of the cubic characteristic equation of the tensor, and from solutions for μ_i in terms of the principal invariants J_i, as described in [21]. We illustrate the structure of Eq. 8 with the eigenvalue wheel in Fig. 1, previously presented by Nickalls [29]. The key insight is that while the mean (μ_1) and variance (μ_2) determine the position and radius of the wheel, respectively, the mode $\sqrt{2}\frac{\mu_3}{\sqrt{\mu_2}^3}$ determines its angular position, which in turn determines the distribution of λ_i. Two eigenvalues can be equal only at the extreme angles of the wheel, $\text{mode} = \pm 1$.

Despite the theoretical interest of mode, the tensor invariant most commonly used in applications of diffusion tensor imaging is *fractional anisotropy* or FA. FA quantifies the extent to which diffusivity is directionally dependent [2]:

$$\text{FA} = \sqrt{\frac{3}{2}}\frac{|\widetilde{\mathbf{D}}|}{|\mathbf{D}|}. \quad (9)$$

3.3 Ridge and Valley Manifolds

The ridges and valleys (collectively, creases) of a scalar field f were defined by Eberly et al. [9] in terms of the gradient $\mathbf{g} = \nabla f$ and Hessian $\mathbf{H}$ of the field. Creases are essentially points where the f is at a local extremum, when constrained to the line or plane defined by one or two eigenvectors of the Hessian. A function is at extrema where its gradient is orthogonal to the constraint surface [24], thus ridges and valleys are where the gradient $\mathbf{g}$ is orthogonal to one or two of the unit-length eigenvectors $\{\mathbf{e}_1, \mathbf{e}_2, \mathbf{e}_3\}$ (with corresponding eigenvalues $\lambda_1 \geq \lambda_2 \geq \lambda_3$) of the Hessian $\mathbf{H}$ [20]:

Ridge Line	$\mathbf{g}\cdot\mathbf{e}_2 = \mathbf{g}\cdot\mathbf{e}_3 = 0$ $\lambda_3, \lambda_2 < 0$
Valley Line	$\mathbf{g}\cdot\mathbf{e}_1 = \mathbf{g}\cdot\mathbf{e}_2 = 0$ $\lambda_1, \lambda_2 > 0$

To filter out insignificant features, the crease strength is assessed by the magnitude of the eigenvalues that are required to be negative or positive for ridges and valleys, respectively [9]. Crease line strength is measured by $-\lambda_2$ (for ridges) and λ_2 (for valleys).

The extraction of crease features of scalar-valued invariants in tensor fields is complicated by the non-linearity of the invariants (e.g., $FA(\mathbf{A} + \mathbf{B}) \neq FA(\mathbf{A}) + FA(\mathbf{B})$). Because differentiation (which is a linear operation) and invariant computation do not commute, one cannot pre-compute the invariants on the regular grid of discrete tensor samples, and then extract crease features. Our experience has been that this has been especially true for mode, which can vary quickly within a single voxel. Thus, an important aspect of our approach is analytically computing the spatial derivatives of invariants. We do this by evaluating the chain rule for the gradient of invariant J in tensor field $\mathbf{D}(\mathbf{x})$:

$$\nabla J = \frac{dJ}{d\mathbf{x}} = \frac{dJ}{d\mathbf{D}} \frac{d\mathbf{D}}{d\mathbf{x}}. \qquad (10)$$

The spatial gradient $\frac{d\mathbf{D}}{d\mathbf{x}}$ of $\mathbf{D}$ is a third-order tensor, which is numerically formed by replacing each coefficient D_{ij} (in the matrix representation of $\mathbf{D}$) by its gradient ∇D_{ij}. The gradient of J with respect to $\mathbf{D}$ is a second-order tensor (like $\mathbf{D}$ itself) can be built up formulaically with the rules of tensor analysis [18]. For example, $\frac{d\,\mathrm{tr}(\mathbf{D})}{d\mathbf{D}} = \mathbf{I}$, $\frac{d\,|\mathbf{D}|}{d\mathbf{D}} = \mathbf{D}/|\mathbf{D}|$, and $\frac{d\,\det(\mathbf{D})}{d\mathbf{D}} = \det(\mathbf{D})\mathbf{D}^{-1}$, which are sufficient to derive tensor-valued gradients of FA and mode [10]:

$$\frac{d\,FA(\mathbf{D})}{d\mathbf{D}} = \sqrt{\frac{3}{2}} \left(\frac{\theta(\mathbf{D})}{|\mathbf{D}|} - \frac{|\widetilde{\mathbf{D}}|\mathbf{D}}{|\mathbf{D}|^3} \right) \qquad (11)$$

$$\frac{d\,\mathrm{mode}(\mathbf{D})}{d\mathbf{D}} = \frac{3\sqrt{6}\theta(\mathbf{D})^2 - 3\mathrm{mode}(\mathbf{D})\theta(\mathbf{D}) - \sqrt{6}\mathbf{I}}{|\widetilde{\mathbf{D}}|} \qquad (12)$$

$$\theta(\mathbf{D}) = \widetilde{\mathbf{D}}/|\widetilde{\mathbf{D}}|. \qquad (13)$$

The product $\frac{dJ}{d\mathbf{D}} \frac{d\mathbf{D}}{d\mathbf{x}}$ in (10) is then computed with tensor contraction [18].

3.4 Smooth Tensor Field Reconstruction

Following previous work in crease extraction in tensor field [20], we apply a convolution-based method of reconstructing a smooth tensor field described, similar to previous work [1, 31]. However, as a consequence of our algorithmic reliance on the locally-linear property of not just the gradient, but also the Hessian eigenvectors, we have found it useful to have C^3-smooth reconstructions, as opposed to the merely C^2 smoothness of cubic B-spline reconstructions. Piecewise polynomial reconstruction kernels of tunable smoothness and accuracy have been studied extensively by Möller et al., and we have selected the approximating C^3 2nd-order accurate filter, which is piece-wise quintic kernel with 4-sample support [26]. From this kernel $q(x)$ we define a separable three-dimensional reconstruction kernel $Q(x,y,z)$

$$Q(x,y,z) = q(x)q(y)q(z) \qquad (14)$$

$$q(x) = \begin{cases} 0 & |x| > 2 \\ 0.1x^5 - 0.75x^4 + 2x^3 - 2x^2 + 0.8 & 1 < |x| < 2 \\ -0.3x^5 + 0.75x^4 - x^2 + 0.7 & 0 < |x| < 1. \end{cases} \qquad (15)$$

The filtering and convolution is computed for each coefficient of the matrix representation of $\mathbf{D}$. We found that extracting the smooth shape of crease features is improved by additionally smoothing the tensor field as a pre-process, as described in Section 5. Spatial derivatives of the convolution-based reconstructions are measured by convolving the data with derivatives of the reconstruction kernel [14].

3.5 Crease Lines and Tensor Structure

The contents of this section can be summarized by noting that the robust and accurate numerical computations enabled by smooth reconstruction kernels permit the application of the well established conceptual framework of crease line extraction to tensor invariants. Furthermore the key observation that topological singularities themselves are ridge and valley lines of tensor mode underscores the generality of this framework and its capacity to identify important structures in tensor fields in different contexts. Further evidence is provided in Section 5

where we successfully extend this idea to FA in DTI data, an application domain where topology is not suitable. The following Section describes the algorithmic solution that allows us to turn this concept into a practical tensor analysis tool.

4 IMPLEMENTATION

In this section we describe the algorithmic aspects involved in the extraction of ridge and valley lines of a tensor invariant on a voxel grid, in which piecewise polynomial kernels provide a smooth reconstruction of the tensor invariant and of its spatial derivatives of first and second-order. Our implementation builds upon a significant body of previous work in the field of scientific visualization, image analysis, and computer vision. Yet, the shortcomings of existing schemes in the specific and challenging case of nonlinear tensor invariants led us to design a new method. For the clarity of the discussion we present in the following the basic ideas underlying our method, which we contrast with alternative techniques.

4.1 Isocontour Approach and Limitations

Following the definitions given in Section 3.3 ridge and valley lines can be defined as the one-dimensional intersection of two 0-isosurfaces of the scalar product between the gradient $\mathbf{g}$ and one eigenvector of the Hessian $\mathbf{e}_i$. With this approach, each isocontour can be computed with commonly used isosurface schemes, *e.g.* *Marching Cubes* [23]. Yet, this solution requires to assign a consistent orientation to the eigenvector field, which is the basic principle of the method proposed by Furst and Pizer [11]. In particular, these authors resolve the orientation ambiguity of eigenvector fields along edges of the voxel by matching their value at both vertices with respect to their average orientation, which is determined by a *Principal Component Analysis* first proposed by Stetten and Pizer [39].

Unfortunately, we found this approach numerically unstable in our experiments, a fact consistent with previous observations [34]. A simple explanation for the rather poor results that we obtained is that the two eigenvectorfields involved in that method are quite often ambiguous. This situation corresponds to the presence of *semi-umbilics* – where two eigenvalues of the Hessian are equal – and indicates a local cylindrical symmetry of the scalar measure. Eberly provides a thorough analysis of this issue [8]. However the method that he proposes to alleviate this problem requires the computation of the third-order derivative of the field (the derivative of the Hessian) to define a *ridge flow*. This vector field is then used in an iterative search to converge towards a crease point on a voxel face starting from a nearby location. In contrast, we have chosen to avoid the complexity of a third-order derivation of our reconstruction kernel in our implementation. A major motivation for doing so was the significant difficulty involved in deriving analytical expression of the third-order derivative of FA or mode in terms of the coefficients of the tensor and their spatial derivatives. We describe in the following our method, in which an efficient and robust adaptive strategy removes the need for third-order derivation.

4.2 Parallel Vector Operator Method

As mentioned in Section 2, the *Parallel Vector Operator* (PVO) [32] offers an alternative to the intersection of two 0-isosurfaces to compute crease points on triangular faces. Namely, the operator can be applied to the gradient and the major (resp. minor) eigenvector of the Hessian to yield the locations where they are aligned. In its general form, the PVO takes two vector fields $\mathbf{v}_0$ and $\mathbf{v}_1$ as input and it determines the locations where $\mathbf{v}_0$ and $\mathbf{v}_1$ are parallel. Note that this latter condition is equivalent to $\mathbf{v}_0 \times \mathbf{v}_1 = \mathbf{0}$ or, alternatively, $\exists \lambda \in \mathbb{R}, \mathbf{v}_0 = \lambda \mathbf{v}_1$ or $\mathbf{v}_1 = \lambda \mathbf{v}_0$. From this definition it follows that the PVO also identifies the locations where either vector field is zero. Moreover, if $\mathbf{v}_0$ and $\mathbf{v}_1$ are 3D vector fields whose restriction to a triangle is linear, the solution of the PVO on that triangle is obtained through an eigensystem [34]. Indeed, by expressing both vector fields in a local parameterization (u,v) of the triangle as $\mathbf{v}_i(u,v) = \mathbf{V}_i(u,v,1)^T$, where $i \in \{0,1\}$ and $\mathbf{V}_i$ is a 3×3 matrix, the PVO solution is obtained by
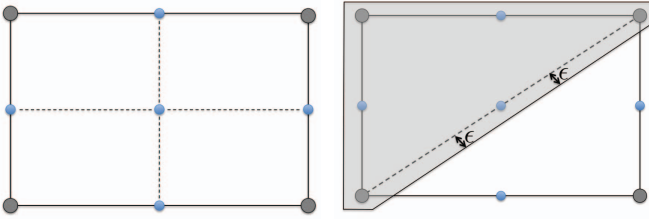
Fig. 2. **Left:** Need for refinement determined by comparing bilinear interpolant based on current resolution (gray vertices) with smooth reconstruction from tensor data at higher resolution (blue vertices). **Right:** PVO is applied to both triangular halves by allowing solutions contained in an ε-neighborhood around each triangle.

solving $\mathbf{V}_0(u,v,1)^T = \lambda \mathbf{V}_1(u,v,1)^T$. If $\mathbf{V}_1$ is invertible, this is equivalent to $\mathbf{V}_1^{-1}\mathbf{V}_0(u,v,1)^T = \lambda(u,v,1)^T$, which is an eigensystem. If $\mathbf{V}_1$ is not invertible but $\mathbf{V}_0$ is, the roles of both vector fields can be swapped. If neither matrix is invertible, the system is singular and an infinite number of solutions exist to the PVO problem [34]. Note that an alternative computation of the PVO solution which does not assume the linearity of the vector fields involves an iterative numerical search. Yet, it requires the computation of the Jacobian of the vector fields, which again in our case would necessitate the third-order derivative of the considered tensor invariant.

In its linear formulation, the PVO can be applied to the gradient and the major (resp. minor) eigenvector of the Hessian matrix. To do so, the considered eigenvector field must first be oriented consistently. Both vector fields are then linearly interpolated over a triangle, which yields the eigensystem mentioned previously. It would therefore seem natural to split the quadrilateral faces of a voxel grid into pairs of triangles and to apply this simple method to each of them. The major drawback of this approach, however, is its assumption of local linearity of the vector fields at play. In our case, this assumption is clearly invalid at the native resolution of the data [19].

4.3 An Adaptive Method

The solution that we propose follows naturally from the remarks made previously. It uses the *PVO* method in its eigensystem formulation but it addresses its requirement of local linearity by applying a local refinement strategy that adjusts the resolution of the analysis to the spatial variations of gradient and eigenvectors of the Hessian. The different steps of our algorithm are described in the following.

4.3.1 Initial filtering

Our method first applies a simple filtering to the data, which discards the voxel faces in which either the considered invariant has non-interesting values (values under a threshold for ridges, values over a threshold for valleys) or its local crease strength (quantified as λ_2, refer to Section 3.3) has an invalid sign (positive for ridges, negative for valleys).

4.3.2 Adaptive refinement

For each remaining voxel face, we assign a coherent orientation to the eigenvectors defined at the four vertices using the PCA method of Stetten [39]. Then we assess the approximation quality of a bilinear interpolation of the gradient and oriented eigenvector fields. This is done by comparing interpolated values with the ground truth provided by direct smooth reconstruction from the tensor field, see Figure 3.4, left.

This comparison is done by measuring the angle between the smooth reconstructed vector and the bilinearly interpolated vector. Note that the vectors are normalized before comparison. A threshold controls the maximal admissible angular discrepancy. This threshold can be adjusted to meet the needs of the extraction. In practice, we initially request a maximal angle of $\frac{\pi}{8}$. If interpolation and reconstruction

disagree, the quadrilateral is recursively split in 4 subfaces. Observe that the values at the resulting vertices have already been computed as part of the approximation quality test. The subdivision stops when the approximation quality criterion is met or a maximal depth has been reached. In both cases, we will process the resulting sub-face without further subdivision. We used a maximum depth of 4 in all our experiments, starting from the native resolution of the grid, while in most cases only 1 or 2 subdivisions were necessary.

4.3.3 PVO method

Once both gradient and eigenvector fields have been found to be properly approximated by low-order interpolation on a given quadrilateral face (or subface), the *PVO* method can be applied to the corresponding pair of triangles. We note that the arbitrary and asymmetric nature of the subdivision in triangles is not problematic in practice since we apply an ε-tolerance to include positions lying in the direct vicinity of their common edge (refer to Figure 2, right) and we subsequently "uniquify" potentially redundant crease points.

4.3.4 Verification

The discrepancy between the local piecewise linear interpolation assumed by the PVO and the smooth but nonlinear underlying measure compels us to verify both the validity and the accuracy of the PVO solutions. To do so we use the smooth reconstruction to obtain both gradient and eigenvector at the found location. Then, we check that either the angle between both vectors is small (as measured by $1 - |\frac{\mathbf{g} \cdot \mathbf{e}}{\|\mathbf{g}\|}|$) or that the magnitude of the gradient is converging towards zero. The former is checked by imposing a tight error bound (0.005 in our experiments). The latter point is controlled by comparing the magnitude of the gradient at the PVO solution to the average magnitude at the vertices of the processed triangle. If the gradient magnitude is only a tiny fraction of the average gradient magnitude in the face, we interpret it as a zero value. In practice, a threshold of 5% worked well in all our experiments. Observe that it is important to be able to identify zero gradient values among the solutions of the *PVO* in cases where the tensor invariant reaches its extremum values (e.g. $-1/+1$ for *mode*). If neither criteria are met by the *PVO* solution, an additional subdivision is applied around the location of the PVO solution to further refine the approximation quality of our local linearization. If the refined solution fails both tests again, the face is discarded.

4.3.5 Connected components

The output of the procedure described above is a point cloud that is further organized with respect to the voxels each point belongs to. We reconstruct connected components from these points by linking pairwise the points found in the faces of a voxel containing exactly two vertices. If the voxel is associated with more than two crease vertices, we simply select the pair associated with the two highest (resp. lowest) values for a ridge (resp. valley). Note that a more sophisticated heuristic could be used, in which multiple crease line segments can be identified by their pairwise signature on the voxel faces and in which the ambiguity of the connectivity can be resolved through internal 3D subdivision of the voxel. If only one point was found on the side faces of a voxel, two situations are possible. Either the crease line stops in this voxel (e.g. because the corresponding value of the invariant becomes non-interesting) or the algorithm described above failed to converge toward a valid crease point. We rule out false negatives by applying our adaptive method on the 5 remaining faces of the voxel at a finer resolution, while doubling the approximation accuracy (i.e. dividing the allowed angle discrepancy by 2). The main benefit of this search a posteriori is that its higher computational cost is strictly limited to the relatively few locations where crease lines are already known to be present. In turn, this feature allows us to work with a rather low resolution of the grid and to apply fairly restrictive filtering criteria in the first stage of the algorithm. Indeed, the only requirement for a crease line to be completely identified by our algorithm is that at least one intersected voxel face fulfills the imposed filtering criteria. The remaining points can then be recovered iteratively.

4.3.6 Tracking

Visualization and image processing methods extracting line features through their pointwise intersection with the faces of a mesh typically try to use a tracking strategy to recover a full curve from a single point. When possible, this one-dimensional marching significantly reduces the computational complexity of the algorithm. Moreover, it permits to disambiguate the connectivity of isolated points on voxel faces. Eberly proposed such a method [7] that was applied recently by Sahner et al. to extract vortex core lines [36]. This method in fact shares deep similarities with the *Feature Flow Field* [40]. Translated to our setting, however, these methods would require the computation of third-order derivatives. In contrast, Zheng et al. proposed a method that computes the tangent of degenerate lines in tensor fields based on the Hessian of the tensor discriminant [43]. Therefore it necessitates only the second-order derivatives of the tensor coefficients.

Using *mode* we can show a very similar result. Indeed, since the degenerate lines of tensor field topology are ridge and valley lines of *mode* associated with global extrema ($+1$ and -1), the gradient of *mode* is uniformly zero along those lines. Moreover, since the minor and medium (resp. medium and major) eigenvalues of the Hessian are by definition both negative (resp. positive) along those lines, it follows from a simple linear analysis that the tangent of the degenerate line is provided by the major (resp. minor) eigenvector of the Hessian of *mode*. Furthermore, the associated eigenvalue is zero. Practically, we use this basic result to integrate along ridge and valley lines of *mode* corresponding to degenerate lines. Starting from a voxel face, we obtain the next intersection point by integrating along the major (resp. minor) eigenvector of the Hessian. To prevent inaccuracies from building up as we iteratively move across multiple voxels, we use the points provided by integration as an approximate location of the crease point and apply a PVO computation to a small neighborhood around it.

5 RESULTS

5.1 Topology of Stress Tensor Fields

As a first application example of our method, we show how it can be used to extract the degenerate lines of the tensor field topology. Specifically, we applied our crease line extraction technique to a synthetic stress tensor field corresponding to a double point load simulation configuration. This tensor field is in fact very similar to the one used by Zheng and Pang in their seminal work on the visualization of degenerate lines [42, 43]. To generate the data, we sample the analytic function of two single point loads [41] on a 256 x 156 x 128 regular mesh spanning a $[-1,1]^2 x[-1,0]$ volume. The two single loads are symmetrically positioned with respect to the center of the top mesh boundary, located at $(-0.5,0,0)$ and $(0.5,0,0)$ respectively. Subsequently, we extract the ridge lines of mode associated with value +1 (corresponding to linear anisotropy, i.e. $\lambda_1 > \lambda_2 = \lambda_3$) as well as the valley lines of mode associated with value -1 (planar anisotropy, $\lambda_1 = \lambda_2 > \lambda_3$). The results are shown in Figure 3.

The structures obtained by our method are remarkably similar to those previously reported in [42, 43]. Note that to compute the degenerate lines of a tensor field we only extract a subset of the crease lines of mode, namely those corresponding to its extremal values of +1 and -1. While other crease lines of mode will typically be present, they will not correspond to degenerate lines and are therefore rejected by our method. Practically, a threshold close to the desired value (+1 or -1) can be applied to determine a small number of voxels that will be investigated. Applying our algorithm to the faces of those voxels yields a number of crease points. In voxels where two crease points were found, their connection provides a local approximation of a degenerate line. In voxels where only one point was found we simply integrate along the major (resp. minor) eigenvector of the Hessian until we intersect the next voxel face. We then iteratively inspect the neighboring voxel that was reached. This tracking continues until either entering a voxel that already contained a single crease point, or the integration along the eigenvector of the Hessian of mode stops within the voxel, indicating the presence of a spherical degenerate point.
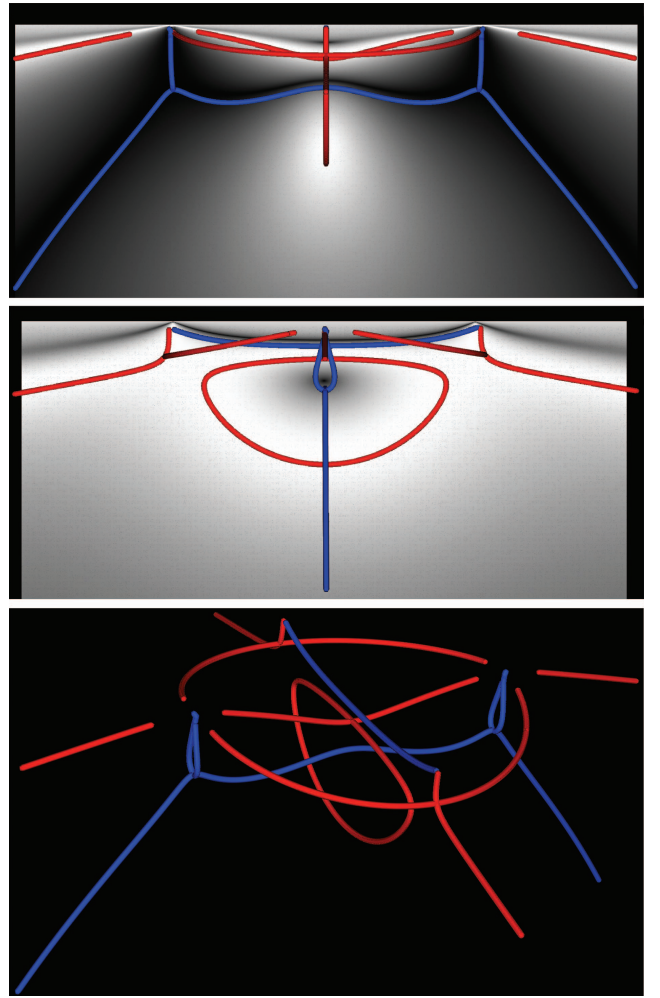

Fig. 3. Lines of planar and linear anisotropy of the topology extracted as ridge (red) and valley (blue) lines of mode with value +1 and -1 respectively from a synthetic shear stress tensor field induced by a symmetric double point load configuration. The top two images show a gray scale colormapping of mode on two orthogonal cross sections.

5.2 Analysis of Brain White Matter in DT-MRI

As mentioned previously, an alternative to the topological definition of tensor structure can be provided by the ridge and valley lines of anisotropy measures in DT-MRI datasets. In fact, Schultz et al. recently showed that topology was unable to reliably characterize structures in DTI data under the presence of noise [38]. On the other hand, previous work on anisotropy crease extraction in DTI suggested the value of FA ridges lines, but never demonstrated their geometric extraction [20]. We demonstrate here the extraction of FA crease lines to model certain significant white matter tracts. The rationale is that the interior points of regions that remain anisotropic even after some smoothing must have orientational coherence, and are thus likely to be fiber bundles. Ridge lines of FA may therefore provide a means of capturing the skeleton of certain white matter bundles.

We extracted ridges lines of FA in a human brain DTI scan with resolution 1.6mm³. Fig. 4 shows the 425 extracted lines with length of at least 15mm, which includes a number of lines of unclear significance. Further thresholding the lines to select only those with the highest average ridge strength (as defined in Sect 3.3), reveals a smaller subset of 62 lines that is explored in the following figures.

Figure 5 shows a similar axial view of the main FA ridge lines, including whole-brain tractography seeded at voxels with FA above
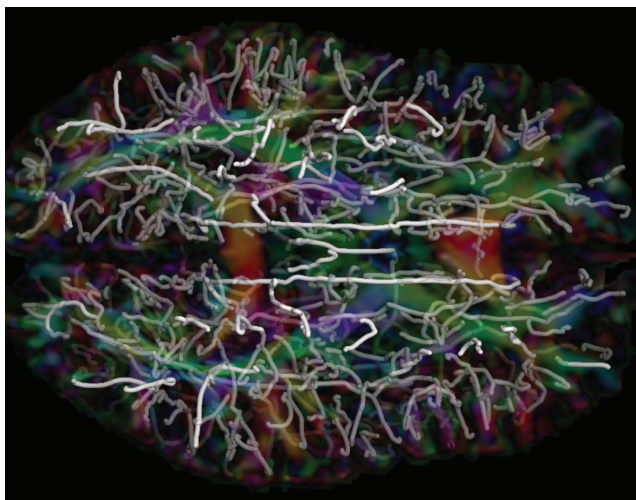
Fig. 4. Axial view of 425 FA ridge lines (length at least 15mm) with RGB-colored cutting plane (both semi-transparent). Thresholding further based on average ridge line strength can reduce the set to the strongest 62 lines (opaque) with more anatomic significance.
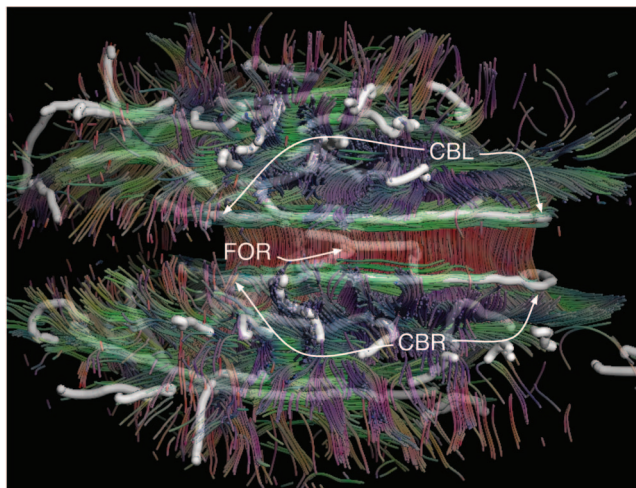

Fig. 5. Axial view of main FA ridge lines, with tractography (semi-transparent). CBL, CNR: left and right cingulum bundles; FOR: fornix.
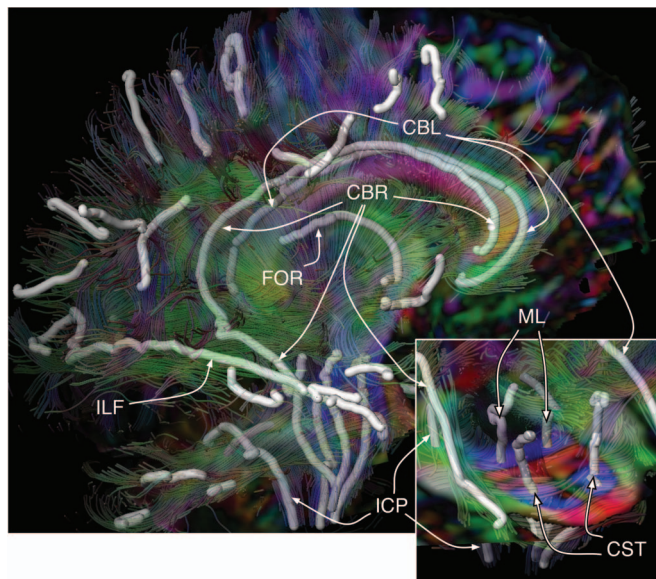

Fig. 6. Sagittal view of main FA ridge lines, with sagittal cutting plane and semi-transparent tractography. Inset shows a more coronal and superior view of the four ascending paths extracted in the midbrain.

tracted fornix (FOR) correctly curves inferiorly (towards the bottom of the image) closer to the front of the brain (right side of image). Also, both CBL and CBR extend fully inferiorly, showing the full loop of the cingulum bundles, which is difficult to capture with conventional tractography. Also annotated Figure 6 is the right inferior longitudinal fasciculus (ILF), which unfortunately was not as cleanly captured on the left side. The inferior cerebellar peduncles (ICP) were well captured (right ICP shown). In the midbrain four additional pathways were captured by FA ridge lines. These are shown in the inset of Fig. 6 with a more coronal and superior viewpoint. The extracted FA ridges lines are mostly centered within the large blue (ascending/descending direction) areas of the axial slice, helping identify the paths as the left and right sides of the medial lemniscus (ML) and cortical spinal tract (CST). While these paths can also be traced with tractography and represented in aggregate by tractograph clustering, our results suggest that some major paths may be extracted more directly as a purely structural property of a smooth FA signal, which we feel is simpler from both a theoretical and algorithmic standpoint.

6 CONCLUSION

We have introduced a new versatile framework for the structural analysis and the visualization of second-order symmetric tensor fields. Following the key observation that the degenerate lines of tensor topology are equivalently characterized as crease and valley lines of a tensor invariant called mode, we have presented an algorithmic solution that allows for the robust and accurate extraction of crease lines of other nonlinear invariants from practical datasets. Our implementation leverages smooth reconstruction kernels and an adaptive refinement strategy to address the challenge posed by this extraction computation in noisy datasets. Our results show that degenerate lines can be identified by our method in a standard engineering benchmark dataset. They also demonstrate that the ridge lines of FA capture important structural properties of the white matter tracts. We find this last point especially remarkable and we wish to further study the anatomical relevance of this crease-based analysis in future work. Future work will also investigate the stability of the crease lines, subject to noise, to optimize the choice of invariants and reconstruction kernels used for crease extraction.

0.72. The FA ridge lines are shown as thick white tubes amidst the semi-transparent thin tractography paths. The left (CBL) and right (CBR) cingulum bundles and part of the fornix (FOR) are annotated. These are the main fiber paths that are more tube-like than sheet-like in the brain white matter [27], so it is fitting that they can be extracted as ridge lines of anisotropy. These paths have previously been extracted via a more involved combination of tractography, clustering, and geometric processing in recent work by O'Donnell et al. [30]. The CBL and CBR ridge lines, for example, follow the general path of the individual tractography traces, but the ridge lines succeed in extracting the fiber bundles as single paths through the core of the structure, rather than as a cluster of tractography paths. Note also that the fornix, as represented by the FA ridge lines, correctly branches into posterior left and right tracts. All of these paths complement other white matter structures (such as the corpus callosum) that have been previously extracted as ridge *surfaces* of FA [20].

Figure 6 shows a roughly sagittal view of the same ridge lines shown in Fig. 5, along with a sagittal cutting plane through the left cingulum bundle (CBL) and semi-transparent tractography. The ex-

ACKNOWLEDGEMENTS

REFERENCES

[1] A. Aldroubi and P. Basser. Reconstruction of vector and tensor fields from sampled discrete data. *Contemporary Mathematics*, 247:1–15, 1999.

[2] P. J. Basser and C. Pierpaoli. Microstructural and physiological features of tissues elucidated by quantitative-diffusion-tensor MRI. *Journal of Magnetic Resonance, Series B*, 111:209–219, 1996.

[3] D. E. Bourne and P. C. Kendall. *Vector Analysis and Cartesian Tensors*. CRC Press, 3rd edition, 1992.

[4] J. C. Criscione, J. D. Humphrey, A. S. Douglas, and W. C. Hunter. An invariant basis for natural strain which yields orthogonal stress response terms in isotropic hyperelasticity. *Journal of Mechanics and Physics of Solids*, 48:2445–2465, 2000.

[5] M. de Saint-Venant. Surfaces à plus grande pente constituées sur des lignes courbes. *Bulletin de la Société Philomathématique de Paris*, pages 24–30, 1852.

[6] T. Delmarcelle and L. Hesselink. The topology of symmetric, second-order tensor fields. In *VIS '94: Proceedings of the conference on Visualization '94*, pages 140–147, Los Alamitos, CA, USA, 1994. IEEE Computer Society Press.

[7] D. Eberly. *Ridges in Image and Data Analysis*. Kluwer Academic Publishers, 1996.

[8] D. Eberly. Theory of ridges. In *http://www.geometrictools.com/Documentation/Ridges.pdf*, 2008.

[9] D. Eberly, R. Gardner, B. Morse, and S. Pizer. Ridges for image analysis. *Journal of Mathematical Imaging and Vision*, 4:351–371, 1994.

[10] D. B. Ennis and G. Kindlmann. Orthogonal tensor invariants and the analysis of diffusion tensor magnetic resonance images. *Magnetic Resonance in Medicine*, 55(1):136–146, 2006.

[11] J. D. Furst and S. M. Pizer. Marching ridges. In *Proceedings of 2001 IASTED International Conference on Signal and Image Processing*, 2001.

[12] J. D. Furst, S. M. Pizer, and D. H. Eberly. Marching cores: A method for extracting cores from 3d medical images. In *Proceedings of IEEE Workshop on Mathematical Methods in Biomedical Image Analysis*, pages 124–130, 1996.

[13] A. Globus, C. Levit, and T. Lasinski. A tool for visualizing the topology if three-dimensional vector fields. In *IEEE Visualization Proceedings*, pages 33 – 40, October 1991.

[14] R. Gonzalez and R. Woods. *Digital Image Processing*. Addison-Wesley Publishing Company, Reading, MA, 2nd edition, 2002.

[15] R. M. Haralick. Ridges and valleys on digital images. *Computer Vision, Graphics, and Image Processing*, 22:28–38, 1983.

[16] J. Helman and L. Hesselink. Surface representation of two and three-dimensional fluid flow topology. In *Proceedings of IEEE Visualization '90 Conference*, pages 6–13, 1990.

[17] L. Hesselink, Y. Levy, and Y. Lavin. The topology of symmetric, second-order 3D tensor fields. *IEEE Transactions on Visualization and Computer Graphics*, 3(1):1–11, 1997.

[18] G. A. Holzapfel. *Nonlinear Solid Mechanics*. John Wiley and Sons, Ltd, England, 2000.

[19] G. Kindlmann, X. Tricoche, and C.-F. Westin. Anisotropy creases delineate white matter structure in diffusion tensor MRI. In *Proceedings of Medical Imaging Computing and Computer-Assisted Intervention, MICCAI '06, Lecture Notes in Computer Science 3749*, 2006.

[20] G. Kindlmann, X. Tricoche, and C.-F. Westin. Delineating white matter structure in diffusion tensor MRI with anisotropy creases. *Medical Image Analysis*, 11(5):492–502, October 2007.

[21] G. L. Kindlmann. *Visualization and Analysis of Diffusion Tensor Fields*. PhD thesis, University of Utah, Sept 2004. Chap 2, http://www.cs.utah.edu/research/techreports/2004/pdf/UUCS-04-014.pdf.

[22] J. Koenderink and A. van Doorn. Local features of smooth shapes: Ridges and courses. In SPIE, editor, *Proc. SPIE Geometric Methods in Computer Vision II, Vol. 2031*, pages 2–13, 1993.

[23] W. E. Lorensen and H. E. Cline. Marching cubes: A high resolution 3d surface construction algorithm. *Computer Graphics*, 21(4):163–169, 1987.

[24] J. E. Marsden and A. J. Tromba. *Vector Calculus*. W.H. Freeman and Company, New York, New York, 1996.

[25] J. Maxwell. On hills and dales. *The London, Edinburgh and Dublin Philosophical Magazine and Journal of Science*, 40(269):421–425, 1870.

[26] T. Möller, R. Machiraju, K. Mueller, and R. Yagel. Evaluation and design of filters using a taylor series expansion. *IEEE Transactions on Visualization and Computer Graphics*, 3(2):184–199, 1997.

[27] S. Mori, S. Wakana, L. Nagae-Poetscher, and P. V. Zijl. *MRI Atlas of Human White Matter*. Elsevier, 2005.

[28] B. S. Morse. *Computation of Object Cores from Grey-Level Images*. PhD thesis, University of North Carolina at Chapel Hill, Chapel Hill, NC, 1994.

[29] R. W. D. Nickalls. A new approach to solving the cubic: Cardan's solution revealed. *The Mathematical Gazette*, 77:354–359, Nov 1993.

[30] L. J. O'Donnell, C.-F. Westin, and A. J. Golby. Tract-based morphometry. In *Tenth International Conference on Medical Image Computing and Computer-Assisted Intervention (MICCAI '07)*, volume 4792 of *Lecture Notes in Computer Science*, pages 161–168, Brisbane, Australia, 2007.

[31] S. Pajevic, A. Aldroubi, and P. J. Basser. A continuous tensor field approximation of discrete DT-MRI data for extracting microstructural and architectural features of tissue. *Journal of Magnetic Resonance*, 154:85–100, 2002.

[32] R. Peikert and M. Roth. The Parallel Vectors operator - a vector field visualization primitive. In *IEEE Visualization Proceedings '00*, pages 263 – 270, 2000.

[33] W. Press, B. Flannery, S. Teukolsky, and W. Vetterling. *Numerical Recipes: The Art of Scientific Computing*. Cambridge University Press, Cambridge, New York, Melbourne, 1986.

[34] M. Roth. *Automatic Extraction of Vortex Core Lines and Other Line-Type Features for Scientific Visualization*. PhD thesis, ETH Zürich, 2000.

[35] F. Sadlo and R. Peikert. Efficient visualization of lagrangian coherent structures by filtered amr ridge extraction. *IEEE Transactions on Visualization and Computer Graphics*, 13(6):1456–1463, 2007.

[36] J. Sahner, T. Weinkauf, and H.-C. Hege. Galilean invariant extraction and iconic representation of vortex core lines. In K. J. K. Brodlie, D. Duke, editor, *Proc. Eurographics / IEEE VGTC Symposium on Visualization (EuroVis '05)*, pages 151–160, Leeds, UK, June 2005.

[37] G. Scheuermann and X. Tricoche. Topological methods in flow visualization. In C. Johnson and C. Hansen, editors, *Visualization Handbook*, pages 341–356. Academic Press, 2004.

[38] T. Schultz, H. Theisel, and H.-P. Seidel. Topological visualization of brain diffusion MRI data. *IEEE Transactions on Visualization and Computer Graphics*, 13(6):1496–1503, 2007.

[39] G. D. Stetten. Medial-node models to identify and measure objects in real-time 3-D echocardiography. *IEEE Transactions on Medical Imaging*, 18(10):1025–1034, 1999.

[40] H. Theisel and H.-P. Seidel. Feature flow fields. In *Proceedings of Joint Eurographics - IEEE TCVG Symposium on Visualization (VisSym '03)*, pages 141–148, 2003.

[41] S. Timoshenko and J. Goodier. *Theory of Elasticity*. 1970.

[42] X. Zheng and A. Pang. Topological lines in 3D tensor fields. In *VIS '04: Proceedings of the conference on Visualization '04*, pages 313–320, Washington, DC, USA, 2004. IEEE Computer Society.

[43] X. Zheng, B. N. Parlett, and A. Pang. Topological lines in 3D tensor fields and discriminant hessian factorization. *IEEE Transactions on Visualization and Computer Graphics*, 11(4):395–407, 2005.